DTU Library

Wireless Photoelectrochemical Water Splitting Using Triple-Junction Solar Cell Protected by TiO$_2$

Moon, Choongman; Seger, Brian; Vesborg, Peter Christian Kjærgaard; Hansen, Ole; Chorkendorff, Ib

Article

Wireless Photoelectrochemical Water Splitting Using Triple-Junction Solar Cell Protected by TiO$_2$

PEC devices integrate a water electrolyzer and solar cell monolithically to promote cost-efficient solar hydrogen production. Moon et al. show a PEC device in a wireless configuration, which would be the idealized architecture. The amount of hydrogen produced over its lifetime reaches 51 mL/cm^2.

Choongman Moon, Brian Seger, Peter Christian Kjærgaard Vesborg, Ole Hansen, Ib Chorkendorff

ibchork@fysik.dtu.dk

HIGHLIGHTS

Wireless PEC device made of triple-junction solar cells protected by TiO$_2$ is tested

Subcell efficiencies depending on TiO$_2$ protection layer thickness are investigated

H$_2$ lifetime reaches 51 mL/cm^2

Article

Wireless Photoelectrochemical Water Splitting Using Triple-Junction Solar Cell Protected by TiO$_2$

Choongman Moon,[1] Brian Seger,[1] Peter Christian Kjærgaard Vesborg,[1] Ole Hansen,[2] and Ib Chorkendorff[1,3,*]

SUMMARY

Photoelectrochemical (PEC) water splitting devices replace electrical contacts in a solid-state solar cell with a solid/liquid junction to improve the solar-to-H$_2$ conversion efficiency and reduce system cost. The wireless configuration can fully use the advantage of the PEC by removing all electrical contacts; however, the wired configuration with the electrical contact on its back side has been widely studied to facilitate device characterization. In this study, a wireless PEC water splitting device made of a commercially available III-V triple-junction solar cell protected by transparent TiO$_2$ is demonstrated with high efficiency and stability. The wireless device produces both H$_2$ and O$_2$ products in a stoichiometric ratio in 13% of solar-to-H$_2$ conversion efficiency over ~12 h, and the total amount of H$_2$ product during the lifetime of the device reaches 51 mL/cm^2, which is the highest value reported from wireless PEC devices to the best of our knowledge.

INTRODUCTION

Photoelectrochemical (PEC) water splitting has been studied over decades as a potential pathway to emission-free hydrogen production.[1,2] The PEC device is made up of a water electrolyzer integrated onto the surface of a solar cell, and photocurrent generated from the solar cell participates in the water splitting reaction on the surface immediately. There have been discussions and techno-economic analyses comparing PEC with electrically wiring separate water electrolyzer and solar cells,[3–5] suggesting that PEC may open the possibility of efficiency improvement and cost reduction by the nature of its device structure. Because the water splitting reaction takes place directly on the solar cell over a large surface area, the low current density flows over a very short distance, which results in low ohmic loss and improved efficiency. Furthermore, PEC does not require power electronics and other intermediary components to combine a solar cell and a water electrolyzer, which would be beneficial for lowering system cost. Shaner et al.[5] conducted a techno-economic analysis on PEC and pointed out that PEC could find economic feasibility, especially when using III-V solar cells with solar concentrators.[6]

PEC devices have mostly been characterized by measuring the photocurrent in a wired configuration in most of the PEC studies. In the wired configuration, one side of the solar cell is connected to an electrical wire or transparent conductive oxide (TCO) while the other side is exposed to an electrolyte. Because of the experimental convenience of current measurement, this wired configuration has become the typical method to investigate the performance. Nevertheless, the advantage of PEC can only be fully realized in a wireless configuration that exposes both sides

[1]Department of Physics, Technical University of Denmark, 2800 Lyngby, Denmark

[2]DTU Nanolab, Technical University of Denmark, 2800 Lyngby, Denmark

[3]Lead Contact

*Correspondence: ibchork@fysik.dtu.dk

https://doi.org/10.1016/j.xcrp.2020.100261

of the solar cell. The wireless configuration can shorten the current flowing distance dramatically because the photocurrent needs to flow only over the thickness of the solar cell. Furthermore, the wireless configuration can reduce system cost by making a stand-alone device without any external components and wiring.[7–9] In spite of the advantages of the wireless configuration, it has not been pursued widely because of the difficulties in characterizing the wireless device. The performance of the wireless device can only be measured by capturing gaseous products in an electrochemical cell with a membrane and tubing without crossover or leakage of the products. The electrochemical cell also needs an elaborate design to minimize the ohmic loss from the proton transport. Moreover, it is more challenging to stabilize a wireless device because both sides of the solar cell are exposed to an electrolyte. Reece et al.[7] realized PEC water splitting in the wireless configuration using a Si-based triple-junction solar cell with 2.5% solar-to-H_2 (STH) conversion efficiency.

There have been many efforts made to improve the stability of PEC in the wired configuration because of the aforementioned experimental convenience,[10–31] but the stability is often evaluated without analyzing the gaseous product.[11,13–17,19,21,24,25,27] The stability is thus only assessed by the evolution of the current density over a certain period, assuming that the faradic efficiency is 100%. However, it is pertinent to be cautious with these results because the current density may be due to unexpected reactions,[32] such as corrosion of solar cells rather than water electrolysis, especially for the anodic half-reaction. Therefore, directly capturing both H_2 and O_2 over the lifetime of the PEC device (H_2 lifetime) is a more reliable approach to examining stability. According to Ben-Naim et al.,[13] the H_2 lifetime of PEC devices must reach at least 100 L/cm^2 to achieve economic feasibility. However, there are still approximately two orders of magnitude difference between the current state-of-the-art PEC and this goal.

In this work, we investigated wireless solar water splitting using a III-V triple-junction solar cell. The cell is made of GaInP/GaAs/Ge junctions with varying band gaps (1.8/1.4/0.7 eV) to absorb photons with different energies. This triple-junction solar cell fully uses the entire solar spectrum, including the infrared region and is able to supply sufficient photovoltage for unassisted solar water splitting. We investigated the PEC devices in both wired and wireless configurations to present the following features: (1) We demonstrate a highly active PEC water splitting device in the wireless configuration by using the III-V triple-junction solar cell.[7] (2) We also test the PEC device in the wired configuration for further characterization. We investigated the effect of the water layer thickness and the TiO_2 protection layer thickness on the performance of PEC devices. (3) The wireless PEC devices show reasonably good stability in acid by protecting the front side with a transparent TiO_2 layer[11,29] and back side with a thick Ti film. When testing the stability of the wireless device, both H_2 and O_2 products are collected to ensure that the cathode and anode are occupied by H_2 evolution reaction (HER) and O_2 evolution reaction (OER), not by other miscellaneous reactions. This PEC device demonstrates 13% of STH efficiency and shows the highest durability among the wireless PEC devices by achieving an H_2 lifetime of 51 mL/cm^2. We then discuss the corrosion mechanism of this specific device and potential approaches to enhance stability.

RESULTS

The Configuration of the PEC Devices

The experimental setup used to test the wireless device is depicted in Figure 1A. The solar cell used in this study was purchased from AZUR SPACE Solar Power GmbH. The compression cell is designed to expose the front and back sides of the solar cell to an acidic electrolyte for HER and OER, respectively. The proton transport
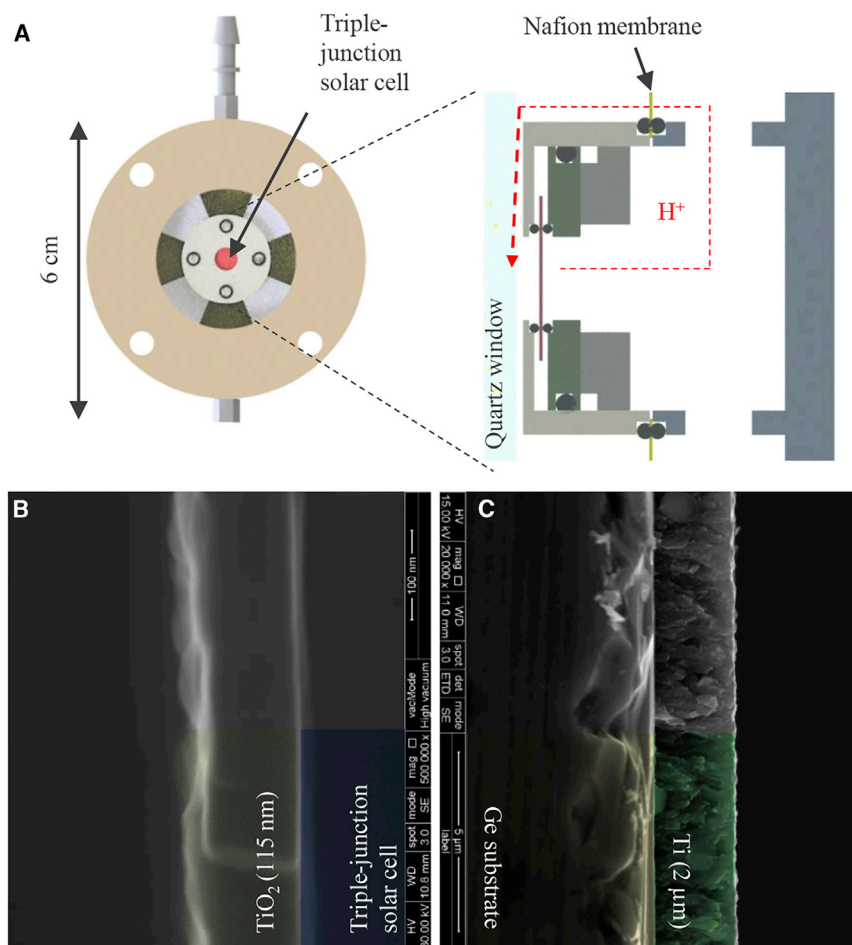
Figure 1. Experimental Setup for Testing Wireless PEC

(A) Compression cell used for testing wireless devices. The red object in the center represents the PEC device. Protons travel from the back side to the front side of the device around the solar cell (along the red dotted line). The design of the compression cell can be further improved by shortening the proton transfer distance.

(B and C) TiO_2 protection layer for the optical front side (B), and (C) metallic Ti protection layer for the Ge back side of the triple-junction solar cell.

distance around the solar cell is minimized to lower the ohmic loss, and a Nafion membrane separates the gaseous products. Due to the sensitive nature of the triple-junction solar cell, both sides of the solar cell require a protection layer for stable operation in an acidic environment, and they also need electrocatalysts for an efficient water splitting. Over the optical front side of the solar cell, a thin layer of metallic Ti (3 nm) is sputtered as an adhesion layer and followed by the deposition of a TiO_2 protection layer with various thicknesses as shown in Figure 1B.[11,29] Pt nanoparticles with 0.5 nm nominal thickness is deposited on the TiO_2 protection layer as a HER catalyst. The opposing Ge back side requires a highly robust protection layer because the anodic potential needed for OER ($\sim$1.8 V versus RHE) creates a highly corrosive environment. To resolve this, we covered the Ge back side with 10 nm of Au as an electrical contact and a 2-μm thick Ti layer as a protection layer, as shown in Figure 1C. On top of the protection layer, 10 nm IrO_2 is deposited as an OER catalyst. A 10-nm layer allows for a continuous TiO_2-IrO_2 interface without the presence of the electrolyte. This approach results in an ohmic contact rather

than a Schottky barrier or an electrolyte-induced depletion layer developing in the TiO_2. This layer is on the back non-irradiated side, thus allowing the $Ti/TiO_2/IrO_2$ to be as thick as necessary without needing to consider any issues relating to optical absorption.

The wired samples have the same structure, with the exception that a Cu wire is attached to the Au layer using Ag paste instead of the 2-μm-thick Ti and IrO_2 layer. The entire sample is covered by epoxy, except for an opening area in the center of the front side ($\sim$0.2 cm^2). Further details about the preparation are described in the Experimental Procedures section.

The Thickness of the TiO_2 Protection Layer and Water Layer Affect the Activity of the PEC Devices

The photocurrent from the triple-junction solar cell is limited by the junction with the lowest current density; therefore, it is important to match the photocurrent from each junction to be similar. In the PEC design, the Ge bottom junction is based on infrared light absorption, and the light is filtered not only by the two cells in front of the Ge cell but also by the water layer in front of the stack. According to the previous theoretical study,[33] the water layer has preferential absorption in the infrared light; thus, it could deteriorate the activity of the Ge bottom junction and mismatch the photocurrent from each junction. To analyze whether infrared absorption by water can result in the Ge bottom cell to be the current limiting cell in the triple-junction stack, we varied the thickness of the water layer in front of the PEC device and monitored performance. The water layer thickness is controlled to be 2, 4 or 8 ± 0.5 mm, and J-V curves are measured under a Xe lamp with a AM 1.5 G filter imitating the ASTM 1.5 G spectrum (see Figure S1A), as shown in Figure 2A. The J-V curve shows a maximum fill factor of 89% when the water layer thickness is $\sim$2 ± 0.5 mm. However, the fill factor decreases to 82% and 71% as the water layer thickness increases to 4 ± 0.5 mm and 8 ± 0.5 mm, respectively. The change of J-V curve is dominated by two different factors[34–36]: (1) the current density limitation by the Ge bottom junction due to the reduced infrared irradiance, and (2) the diode behavior of the Ge bottom junction in the breakdown region. At the higher potential range ($\sim$1.5 V versus RHE), the increased water layer thickness reduces the infrared light intensity by absorption, and the current density from Ge bottom junction decreases; 4 ± 0.5 mm or 8 ± 0.5 mm of the water layer is able to decrease the current density. However, the current density increases again at the lower potential range ($\sim$0 V versus RHE). The Ge bottom junction is a p-n diode under electrical bias, and the total electrical bias applied on the Ge bottom junction is the sum of external bias from a potentiostat and the photovoltages from the top and middle junction in this PEC experiment. The direction of the external bias and photovoltages are forward and reverse to the p-n junction, respectively. When the external bias is small ($\sim$0 V versus RHE), the total electrical bias on the Ge diode is in the reverse direction and surpasses the breakdown voltage of the Ge diode. In this case, the Ge bottom junction does not limit the current density; thus, the top or middle junction will limit the current density. To test the hypothesis, we illuminated with an additional infrared light by using a tungsten halogen lamp filtered by a Si wafer. The band gap of Si (1.1 eV) allows additional intensity only for the Ge bottom junction (since hv < 1.1 eV). When supplying this additional infrared intensity to the device with 8 ± 0.5 mm of the water layer, the fill factor recovers, and this confirms that Ge bottom junction is limiting the current density at the higher potential range ($\sim$1.5 V versus RHE) in this case.

The photocurrent density of multi-junction solar cells is always limited by the junctions with the lowest current density. Therefore, determining the current limiting
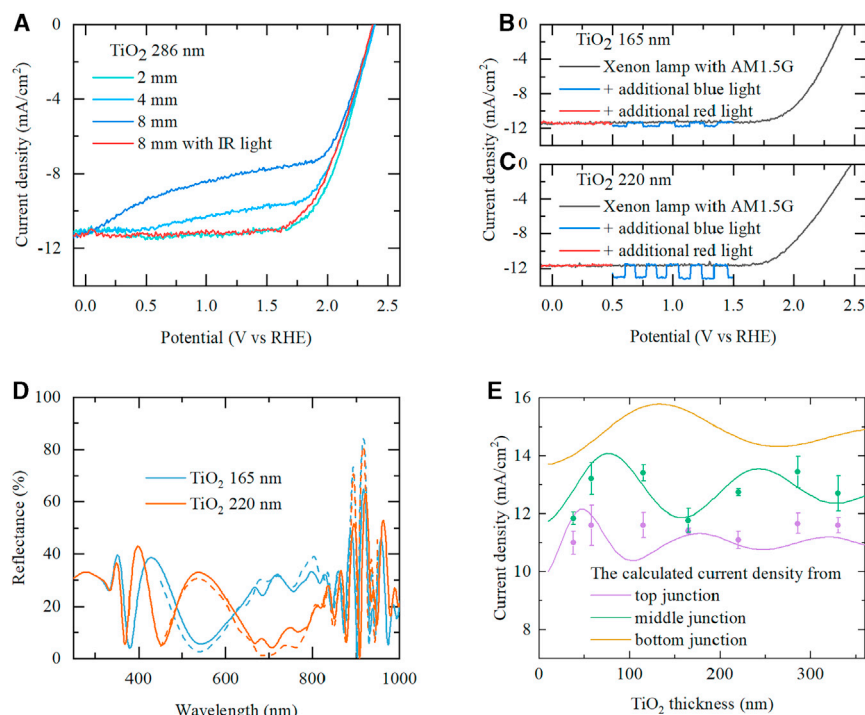
Figure 2. The Thickness of the TiO₂ Protection Layer and Water Layer Affect the Activity of the PEC Devices

(A) The photocurrent density measured with 2, 4, or 8 mm water layer in front of the PEC device. The loss by the infrared absorption is recovered by supplying additional infrared light.

(B and C) Photocurrent density from the triple-junction PEC devices with (B) 165 and (C) 220 nm of TiO₂ thickness (black lines). A chopped source of extra photons for the top junction (blue) and the middle junction (red) are supplied to determine the current limiting junction. See also Figure S2.

(D) The wavelength-dependent reflection of the PEC device for 2 selected TiO₂ thicknesses. The solid lines are calculated, and the dashed lines are measured reflectance. See also Figure S4.

(E) Measured current density without (purple data points) and with (green data points) the blue light is compared to the calculated current density from each junction. The error bars represent the standard deviation from measurements on 3 devices with the same TiO₂ thickness.

junction, and if possible, figuring out the current density from each junction would be valuable information for optimizing a PEC device as it has been done for conventional multi-junction solar cells.[37,38] As shown in Figure 2A, increasing the current density from the Ge bottom junction by supplying the additional intensity in the infrared range cannot make the total current density larger than 11.3 mA/cm², which means that the top or middle junction is limiting the current density to this value. To determine the current limiting junction, we added another light source for either the top or middle junction to the experimental setup. The purpose of the additional light source was to supply photons for one of the junctions exclusively, and the current density should increase when the photons for the current limiting junction is supplied from the additional light source. We used an additional Xe lamp with optical filters to illuminate only the top junction (blue light, 400–500 nm) and the middle junction (red light, 645–900 nm) (see Figure S1B). We measured the photocurrent density of the wired PEC devices with various TiO₂ thicknesses (see Figure S2), and 2 devices with 165 and 220 nm of TiO₂ are shown as representative examples in the gray graph in Figures 2B and 2C. The blue and red graphs in Figures 2B and 2C show the photocurrent density when turning on and off the additional blue and red light, respectively. Both PEC devices with 165 and 220 nm of TiO₂ are showing improved current density when supplying more photons for the GaInP top junction, and this indicates

that the top junction is the current limiting junction. The current density under the additional blue light is not changed in the range of blue light intensity used in this study (see Figure S3 for details). This result implies that the intensity of the additional blue light is large enough to fully saturate the GaInP top junction so that the top junction is not the current limiting junction under the blue light any longer. Furthermore, the blue light intensity is not too high so as to invoke a detectable amount of photoluminescence coupling effect.[39]

Under the blue light illumination where the top junction is not limiting, the middle or bottom junction should be the current limiting junction. However, we can exclude the bottom junction and thus know that the middle junction is the current limiting junction based on the fill factor. As shown in Figure 2A, the current limiting bottom junction can decrease the current density only at ~1.5 V versus RHE, while the current density at the lower potential range remains the same. However, when considering that the current density under the blue light (the blue graphs in Figures 2B and 2C) shows the same current density at 0.5 V versus RHE and 1.5 V versus RHE, the cyclic voltammetry measurement shows a clear difference from the PEC device with the current-limiting bottom junction. Therefore, the current density under the blue light should show the current density from the middle junction. It is noteworthy to observe that the current density from the middle junction clearly differs for the two thicknesses of the TiO_2 layer. The middle junction current density from the PEC device with 165 and 220 nm TiO_2 are 11.8 and 13.2 mA/cm^2, respectively. To explain the thickness dependence, the reflectance of PEC devices with various TiO_2 thicknesses is measured in the visible light range in air (see Figure S4), and 2 representative devices with 165 and 220 nm of TiO_2 are shown in Figure 2D. As the TiO_2 thickness changes, the reflectance of PEC devices also changes and will affect the photocurrent density from each junction.[40] Because the device with 165 nm of TiO_2 has a more significant reflection in the wavelength range for the middle junction (650–900 nm) compared to the device with 220 nm of TiO_2, it has a lower current density from the middle junction.

To quantify the effect of TiO_2 thickness on the reflectance and the current density, the expected photocurrent density from each junction is calculated by taking into consideration the spectral intensity of the light source provided by the supplier, absorption by the water layer,[41] optical properties of materials,[42–44] and internal quantum efficiency derived from the measured external quantum efficiency and reflectance. The thickness of the water layer, which significantly affects the current density from the bottom junction, is assumed to be 2 mm. Further details regarding the current density calculation are described in Note S1. The purple, green, and yellow lines in Figure 2E represent the calculated current densities from the top, middle, and bottom junctions, respectively. The periodic changes of the calculated current density over the TiO_2 thickness are from the optical interference inside the TiO_2 film. When the thickness of the TiO_2 layer satisfies Equation 1, destructive interference will occur for the reflecting wave, and the TiO_2 protection layer will work as an antireflective coating[45]:

$$d = \left(\frac{1}{4} + \frac{1}{2}m\right)\frac{\lambda}{n} \qquad \text{(Equation 1)}$$

where d, m, λ, and n represent TiO_2 thickness, any integer number, the wavelength of light in vacuum, and the refractive index of TiO_2, respectively. This equation shows that the periodic change of the expected current density over TiO_2 thickness depends on the wavelength corresponding to each junction. Because the wavelength of light absorbed from each junction increases in the order of top, middle, and

bottom junction, the periodicity also increases in the same order, as shown in the solid lines in Figure 2E.

The calculated current density from each junction is compared to the experimental measurement. According to the calculation results shown in Figure 2E (solid lines), the GaInP top junction is expected to limit the current density for all TiO_2 thicknesses according to the calculation result because the junction with the lowest current density will limit the current density of entire PEC devices. We measured the photocurrent density from PEC devices with various TiO_2 thicknesses (see Figures 2B, 2C, and S2) and confirmed the current limiting junction by using the additional light sources. As expected from the calculation, all of the PEC devices with the various TiO_2 thicknesses show improved current density under the blue light, which means that the top junction limits the current density. The measured current densities from all of the PEC devices are shown in Figure 2E. The purple data points are measured without the additional blue light, while the green data points are measured with the blue light. Because the PEC devices show improved current density when adding the additional blue light, which is exciting only the top junction, the top junction is the current limiting junction for all devices. Therefore, as explained with Figures 2B and 2C, the purple data points without the blue light represent the current density from the top junction. Also, because the cyclic voltammetry with the additional blue light does not show the characteristic behavior of the bottom junction limiting device (shown in Figure 2A), the green data points represent the current density from the middle junction. All of the data points with error bars are acquired by measuring three independent PEC devices with the corresponding TiO_2 thickness. The measured and calculated current densities from each junction are in accordance with each other. It shows that the current density from each junction in a multi-junction solar cell can be measured with additional light sources, which would be useful information for optimizing a PEC device.

The current density from the PEC device is limited by the top junction, and it is related to the design and optical losses of the device. The triple-junction solar cell used in this study is optimized to operate under AM 0 spectrum with 17.0 mA/cm^2 of current density; however, this study uses the light source-simulating AM 1.5 G spectrum. The difference between the AM 0 and the AM 1.5 G spectrum results in the current limiting top junction generating 13.6 mA/cm^2. There seem to be parasitic losses, which reduces the current density by <1 mA/cm^2, possibly from optical absorption by the Pt catalyst, the TiO_2 protection layer, and the metallic Ti adhesion layers. The device without any reflection would generate 12.6 mA/cm^2, but the loss by reflection results in 10.0–12.1 mA/cm^2 of current density from the top junction, as shown in Figure 2E.

The Stability of the PEC Devices Is Tested by Capturing Gaseous Products over Their Lifetime

The stability of PEC devices is often evaluated by conducting chronoamperometry over a certain period, and the previous work from Ben-Naim et al.[13] provides a framework to indicate the stability of PEC devices by using H$_2$ lifetime (see Figure 4 in Ben-Naim et al.[13]). Figure 3A shows the H$_2$ lifetime from selected works[8,13,22,40,46–55] (circle) as well as this study (rectangle), measured by the total amount of charge passed (see Table S1 for details). The unit of the charge passed (coulombs) is converted to an equivalent amount of H$_2$ for a more relatable figure of merit. The most stable device from this study has 277 nm of the TiO_2 protection layer and produced 231 mL/cm^2 supposing that all of the charges are participating in the water splitting reaction, as depicted in the inset of Figure 3A. However, a large amount of total passed charge does not necessarily mean that the photoelectrode is
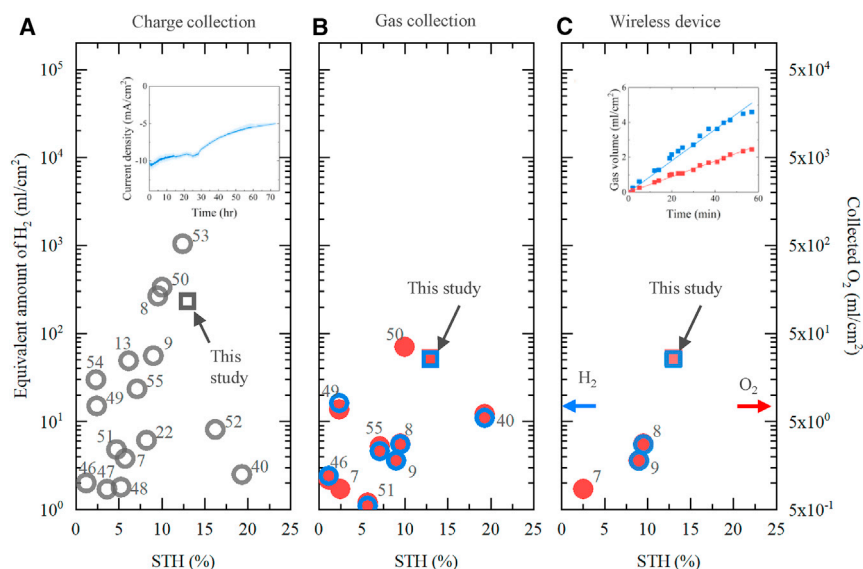
Figure 3. The Stability of the PEC Devices Is Tested by Capturing Gaseous Products over Their Lifetime

Total amount of H_2 produced over the lifetime of PEC devices from selected papers (circle) and this study (rectangle) are charted, depending on the measurement methods.

(A) H_2 lifetime production "measured" by the charge passed in the unit of the equivalent amount of H_2. The wired device from this study reached 231 mL/cm², and the inset figure shows the chronoamperometry data from the device.

(B) H_2 lifetime production measured by gas collection. Blue and red data points represent the amount of collected H_2 (left y axis) and O_2 (right y axis). Note that the H_2 axis is scaled by a factor of 1/2 compared to the O_2 axis to make H_2 and O_2 data points in the stoichiometric ratio (2:1) overlap each other.

(C) H_2 lifetime measured from wireless devices only. The inset figure shows gas collection during the first hour of this study used to calculate STH efficiency.

See also Table S1.

producing H_2 and O_2. As pointed out by the previous study,[32] the current density may originate from the dissolution of semiconductors or other non-water splitting reactions. Therefore, we isolated the data points that collected the gas product among the references in Figure 3A, and showed these more thorough experiments in Figure 3B. The volume of collected H_2 and O_2 is depicted as the blue and red data points, respectively, with the H_2 data point corresponding to the left y axis scale and the O_2 evolution data points corresponding to the right y axis scale. We emphasize that the H_2 axis is scaled by a factor of 1/2 compared to the O_2 scale; thus, if the $H_2:O_2$ ratio is the theoretical value of 2, the H_2 and O_2 data points should be on top of each other. This scaling allows us to easily see whether a given device was truly splitting water or the extent to which a corrosion reaction or something else was involved. The square data point represents the wireless PEC device with 355 nm of TiO_2 from this study (see Video S1). The STH efficiency of the device is 13% based on the amount of gas collected during the first hour of the operation (inset of Figure 3C). The activity of the wireless device is almost the same as that of the wired device in this lab-scale experiment with a small current. The advantage of a wireless device by reducing ohmic loss from electron conduction would be more substantial at a larger-scale device with a larger current. The H_2 lifetime reaches 51 mL H_2/cm², and the ratio between H_2 and O_2 is 2:1 in the range of significant figures of eudiometers (graduation size: 50 μL), which shows that HER and OER are dominant reactions. Figure 3C collects data points from wireless devices only. As we mentioned before, the wireless configuration would be the simplest configuration possible for

PEC and, therefore, attractive for a practical application. To the best of our knowledge, this is the highest value measuring isolated H_2 and O_2 gas among the wireless devices evaluated in an acidic environment.

After stability tests, we investigated the corrosion mechanism of this specific PEC device. It was discovered that wireless samples have severe corrosion only on the front side (i.e., cathode), whereas the back side (i.e., anode) does not show any observable corrosion. This is probably because a 2-μm Ti film is sufficiently thick to prevent the formation of any pinholes that may otherwise lead to local corrosion. However, the corrosion on the front side was clearly observed through scanning electron microscopy (SEM) and energy-dispersive X-ray spectroscopy (EDS). In the initial stages of corrosion, the PEC devices usually show dark spots in SEM, as shown in Figure 4A. Those spots are typically ∼0.1–1 μm and have lower In and P signals and higher arsenic signals in EDS (Figure 4C). The EDS data imply that the GaInP top junction corrodes partially in the spots, leaving the GaAs middle junction exposed. This corrosion could be related to the decrease in current density and photovoltage (see Figure S5 for details) by losing some part of the top junction. In the later stage of corrosion (Figures 4B and 4D–4G), the acidic electrolyte reaches and begins to dissolve the GaAs middle junction. In addition, cracks appear surrounding the initial corrosion spot, possibly because of the faster etch rate of GaAs compared to that of GaInP. X-ray photoelectron spectroscopy (XPS) measurements before and after the stability test show the deposition of dissolved materials (see Figure S6). After the stability test, the arsenic peak is much larger than the P peak, and it also supports the different etch rates between the GaInP top junction and GaAs middle junction. Figures 4H and 4I depict the suggested corrosion process. In Figure 4H, the initial corrosion takes place due to a pinhole in the protection layer. As the corrosion enlarges, the acidic electrolyte contacts the GaAs middle junction, which is more vulnerable to acid than GaInP, and wide areas underneath the top junction are dissolved. It causes cracks along the crystalline orientation of the top junction surrounding the initial corrosion spot, and the cracks eventually lead to delamination.

DISCUSSION

Further improvement of the PEC device is made possible by ensuring less reflection in the broad range of wavelengths for all junctions. The TiO_2 protection layer used in this study works as a monolayer antireflective coating, which is not suitable for reducing the reflection over a broad spectral range. Antireflection in a broad range could be achieved by using a bilayer or multilayer structure made of two materials with different refractive indexes just as the antireflective coating used for conventional solar cells. A certain combination of transparent, conductive, and acid-stable materials could be used for the purpose. Such materials could be prepared by, for example, adding dopants to or changing the crystallinity of TiO_2. A careful control on the thicknesses of multilayers made of such materials can lower the reflectance of the protection layer.

An ideal protection layer for the cathodic side of a PEC device should be stable, transparent, conductive, and impermeable to electrolytes.[56] Sputtered or atomic layer deposition (ALD) TiO_2 is a large band gap n-type material whose conduction band is aligned closely with the hydrogen redox potential.[29,57] These properties make TiO_2 suitable for the electron-conducting protection layer for photocathodes. However, TiO_2 prepared by sputter or ALD is not entirely impermeable to an electrolyte because of pinholes in the protection layer. We presume that the pinholes are created by either the grain boundary of TiO_2 or small dust particles sitting on the surface before TiO_2 deposition.
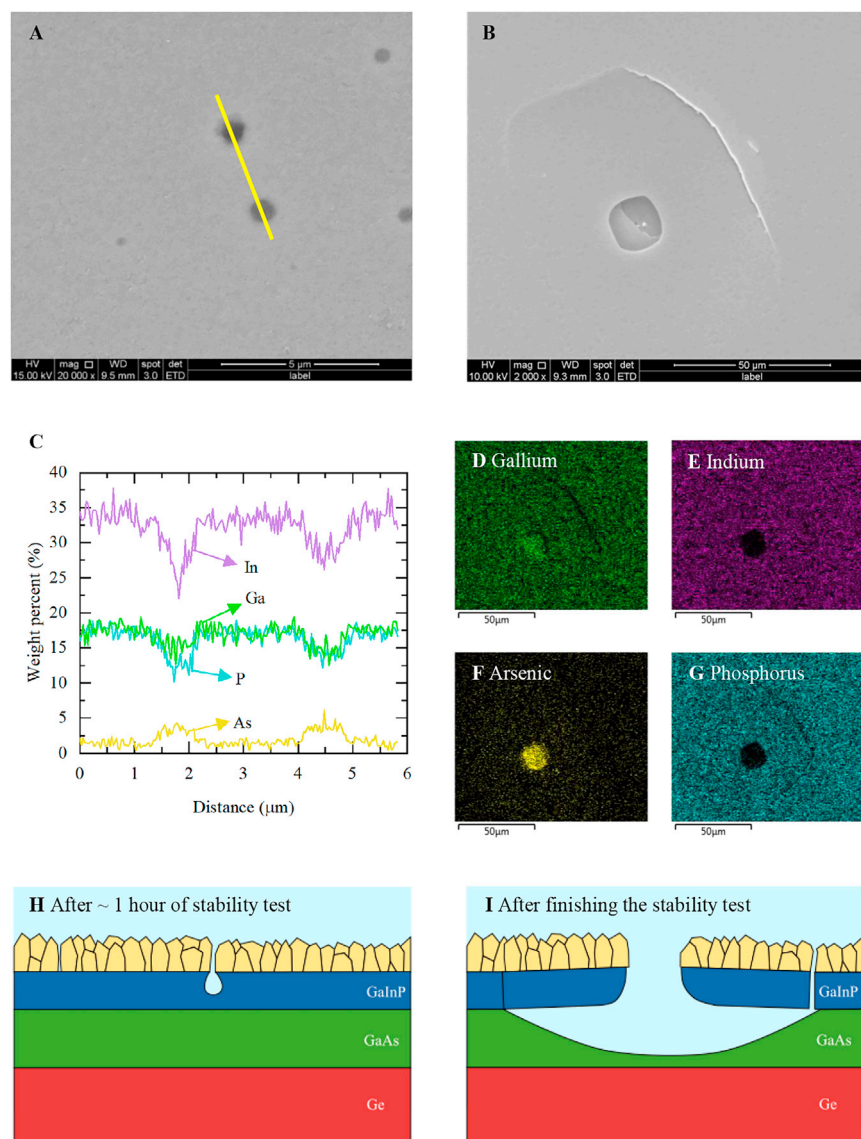
Figure 4. The Surface Morphology of the PEC Devices Is Observed after the Reaction Using SEM and EDS

(A and C) In the initial stage of corrosion, dark spots appear in the SEM image (scale bar: 5 µm). Those spots have a lower composition of top junction materials (In and P) and a higher composition of middle junction materials (As).

(B and D–G) In the later stage of corrosion, the cracks surrounding the corrosion spot appear as shown in the SEM image (scale bar: 50 µm).

(H and I) Schematic diagrams of the corrosion process. Because of a pinhole in the protection layer, the GaInP top junction begins to corrode in the initial stage. When the corrosion in the top junction reaches the GaAs middle junction, the corrosion grows rapidly along the middle junction, and it eventually leads to the delamination of the top junction.

There are potential strategies suggested to improve the stability of PEC devices. For example, pinholes in the protection layer could be reduced or eliminated by improving film quality. Our previous study showed that high-power impulse magnetron sputtering (HiPIMS) can deposit TiO_2 thin films with higher mass density compared to a direct current (DC) magnetron sputtering, which reduces the size and number of pinholes in TiO_2 protection layers. This significantly improves the

stability of Si photocathodes tested in KOH. Similarly, epitaxial deposition of the protection layer could improve stability by removing pinholes and preventing any contact with electrolytes.[21,26]

EXPERIMENTAL PROCEDURES

Resource Availability

Lead Contact

Further information and requests for resources and materials should be directed to and will be fulfilled by the Lead Contact, Ib Chorkendorff (ibchork@fysik.dtu.dk).

Materials Availability

This study did not generate new unique materials.

Data and Code Availability

The experimental data and calculation code generated in this study are available from the Lead Contact upon request.

PEC Device Preparation

We prepared the PEC devices in an International Organization for Standardization (ISO) class 5 cleanroom to reduce contamination during the preparation. The solar cell used in this study was purchased from AZUR SPACE Solar Power GmbH. As-purchased wafers were cleaned by sonication in ethanol and water for 2 min each, rinsing in 1 M HCl for 2 min and water for 5 min. The back side of the solar cell (p-Ge substrate) was cleaned by Ar sputtering once more and covered with 10 nm of Au in a sputter chamber to provide an electrical contact. Au was chosen as the contact layer because Au will form an ohmic contact with p-type Ge by Fermi level pinning nearby to the valence band edge of Ge[58–60] and would not be oxidized during sample preparation. After the Au deposition, 2 μm Ti was deposited on top of the Au layer using an e-beam evaporator. Before the deposition on the front side, the wafer was treated in a mixture of citric acid solution (50 wt%) and hydrogen peroxide (30%) in a 5:1 ratio for 3 min.[61] The front side of the solar cell was covered by 3 nm metallic Ti and the controlled thickness of TiO_2 deposited at 250°C using ALD. The wafer was diced using a diamond saw. To prevent damage to the solar cell junctions, the cutting started from the back side of the wafer (Ge substrate), and the depth of cutting was 80 μm, which is approximately half of the total thickness of the wafer (150 μm). The tessellated wafer was cleaved into small pieces (1 cm^2). Before performing the PEC experiments, 0.5 nm of Pt and 10 nm of IrO_2 were deposited on the front and back sides of the sample as HER and OER catalysts, respectively.

The preparation procedure for a wired sample is the same as the wireless sample until Au deposition. After Au deposition, the wafer was diced into small pieces (1 cm^2). Then, the Ti, TiO_2, and Pt layers were deposited successively using a sputter deposition with a shadow mask to prevent the deposition of materials on the edge-side of the wafer. The back side covered by the Au layer was connected to a Cu wire using Ag paste. The Cu wire and the wafer were encapsulated in a glass tube and epoxy (Loctite Hysol 1C) with an opening area in the front side ($\sim$0.2 cm^2). The Cu wire led to a counter electrode, which was prepared by soaking an Au mesh into 1 mM $IrCl_3$ and annealed in air at 400°C.

Characterization

The light source used in this study was a Xe lamp with an AM 1.5 G filter (Oriel). The spectral intensity of the light source was measured using a spectrophotometer

(Ocean Optics, USB4000-UV-vis [ultraviolet-visible]). We calibrated the light intensity integrated over the detectable wavelength range to be the same as the standard AM 1.5 G spectrum in the same range (68.4 mW/cm^2 in 300–900 nm; see Figure S1A). The reflectance and thickness of the TiO_2 films were measured by ellipsometry, and the surface morphology was observed using SEM and EDS.

The wired devices are investigated in a three-electrode setup. The electrolyte was 0.1 M $HClO_4$ (pH 1), the OER counter electrode was IrO_2 deposited on a gold mesh, and the reference electrode was Hg/Hg_2SO_4. The stability of the wired samples was examined by chronoamperometry at 0 V versus IrO_2. The performance of the wireless samples was measured in a compression cell filled with 1 M $HClO_4$ (pH 0). The design of the compression cell is depicted in Figure 1A. The compression cell was a two-compartment cell separated by a Nafion 117 membrane. The electrolyte in H_2 and O_2 compartments was saturated by H_2 and O_2, respectively. The surface area of the PEC device opened to the electrolyte was 0.2 cm^2, and the thickness of the water layer was kept to ~1 mm to minimize the loss by infrared absorption. The ohmic resistance inside the cell was measured at 48 ohms (see Figure S7A), and it led to 90–100 mV ohmic voltage drop. Each compartment has a connection to a eudiometer (graduation size: 50 µL, total volume: 25 mL) for capturing gas products. Before testing samples in the compression cell, the sample surface was cleaned with O_2 plasma in a vacuum chamber and kept under UV light in air to remove organic contamination. The cleaning process makes the surface hydrophilic and facilitates bubble removal through the shallow water layer. We also carried out a leak test to determine the loss by leakage or crossover of the product by using a thin eudiometer (graduation size: 10 µL, total volume: 1 mL). The expected amount of products from 0.2 cm^2 of the active area was ~1 mL H_2 and 0.5 mL O_2 over 1 h, and this leakage was found to be <1% of the expected amount of products (~10 and ~5 µL/h for H_2 and O_2 compartments each).

SUPPLEMENTAL INFORMATION

ACKNOWLEDGMENTS

AUTHOR CONTRIBUTIONS

C.M. carried out the device preparation, characterization, and calculation. B.S., P.C.K.V., O.H., and I.C. conceived the concept and co-wrote the paper. All of the authors contributed to the discussion and interpretation of the results.

DECLARATION OF INTERESTS

The authors declare no competing interests.

REFERENCES

1. Walter, M.G., Warren, E.L., McKone, J.R., Boettcher, S.W., Mi, Q., Santori, E.A., and Lewis, N.S. (2010). Solar water splitting cells. Chem. Rev. 110, 6446–6473.

2. Bae, D., Seger, B., Vesborg, P.C.K., Hansen, O., and Chorkendorff, I. (2017). Strategies for stable water splitting via protected photoelectrodes. Chem. Soc. Rev. 46, 1933–1954.

3. Ardo, S., Fernandez Rivas, D., Modestino, M.A., Schulze Greiving, V., Abdi, F.F., Alarcon Llado, E., Artero, V., Ayers, K., Battaglia, C., Becker, J.P., et al. (2018). Pathways to electrochemical solar-hydrogen technologies. Energy Environ. Sci. 11, 2768–2783.

4. Pinaud, B.A., Benck, J.D., Seitz, L.C., Forman, A.J., Chen, Z., Deutsch, T.G., James, B.D., Baum, K.N., Baum, G.N., Ardo, S., et al. (2013). Technical and economic feasibility of centralized facilities for solar hydrogen production via photocatalysis and photoelectrochemistry. Energy Environ. Sci. 6, 1983–2002.

5. Shaner, M.R., Atwater, H.A., Lewis, N.S., and McFarland, E.W. (2016). A comparative technoeconomic analysis of renewable hydrogen production using solar energy. Energy Environ. Sci. 9, 2354–2371.

6. Dumortier, M., and Haussener, S. (2015). Design guidelines for concentrated photo-electrochemical water splitting devices based on energy and greenhouse gas yield ratios. Energy Environ. Sci. 8, 3069–3082.

7. Reece, S.Y., Hamel, J.A., Sung, K., Jarvi, T.D., Esswein, A.J., Pijpers, J.J.H., and Nocera, D.G. (2011). Wireless solar water splitting using silicon-based semiconductors and earth-abundant catalysts. Science 334, 645–648.

8. Verlage, E., Hu, S., Liu, R., Jones, R.J.R., Sun, K., Xiang, C., Lewis, N.S., and Atwater, H.A. (2015). A monolithically integrated, intrinsically safe, 10% efficient, solar-driven water-splitting system based on active, stable earth-abundant electrocatalysts in conjunction with tandem III-V light absorbers protected by amorphous TiO_2 films. Energy Environ. Sci. 8, 3166–3172.

9. Varadhan, P., Fu, H.C., Kao, Y.C., Horng, R.H., and He, J.H. (2019). An efficient and stable photoelectrochemical system with 9% solar-to-hydrogen conversion efficiency via InGaP/GaAs double junction. Nat. Commun. 10, 5282.

10. Azevedo, J., Tilley, S.D., Schreier, M., Stefik, M., Sousa, C., Araújo, J.P., Mendes, A., Grätzel, M., and Mayer, M.T. (2016). Tin oxide as stable protective layer for composite cuprous oxide water-splitting photocathodes. Nano Energy 24, 10–16.

11. Bae, D., Shayestehaminzadeh, S., Thorsteinsson, E.B., Pedersen, T., Hansen, O., Seger, B., Vesborg, P.C.K., Ólafsson, S., and Chorkendorff, I. (2016). Protection of Si photocathode using TiO_2 deposited by high power impulse magnetron sputtering for H_2 evolution in alkaline media. Sol. Energy Mater. Sol. Cells 144, 758–765.

12. Benck, J.D., Lee, S.C., Fong, K.D., Kibsgaard, J., Sinclair, R., and Jaramillo, T.F. (2014). Designing active and stable silicon photocathodes for solar hydrogen production using molybdenum sulfide nanomaterials. Adv. Energy Mater. 4, 1–8.

13. Ben-Naim, M., Britto, R.J., Aldridge, C.W., Mow, R., Steiner, M.A., Nielander, A.C., King, L.A., Friedman, D.J., Deutsch, T.G., Young, J.L., et al. (2020). Addressing the Stability Gap in Photoelectrochemistry: Molybdenum Disulfide Protective Catalysts for Tandem III–V Unassisted Solar Water Splitting. ACS Energy Lett. 5, 2631–2640.

14. Britto, R.J., Benck, J.D., Young, J.L., Hahn, C., Deutsch, T.G., and Jaramillo, T.F. (2016). Molybdenum Disulfide as a Protection Layer and Catalyst for Gallium Indium Phosphide Solar Water Splitting Photocathodes. J. Phys. Chem. Lett. 7, 2044–2049.

15. Chen, Y.W., Prange, J.D., Dühnen, S., Park, Y., Gunji, M., Chidsey, C.E.D., and McIntyre, P.C. (2011). Atomic layer-deposited tunnel oxide stabilizes silicon photoanodes for water oxidation. Nat. Mater. 10, 539–544.

16. Choi, M.J., Jung, J.Y., Park, M.J., Song, J.W., Lee, J.H., and Bang, J.H. (2014). Long-term durable silicon photocathode protected by a thin Al_2O_3/SiO_x layer for photoelectrochemical hydrogen evolution. J. Mater. Chem. A Mater. Energy Sustain. 2, 2928–2933.

17. Fan, R., Dong, W., Fang, L., Zheng, F., Su, X., Zou, S., Huang, J., Wang, X., and Shen, M. (2015). Stable and efficient multi-crystalline n+p silicon photocathode for H_2 production with pyramid-like surface nanostructure and thin Al_2O_3 protective layer. Appl. Phys. Lett. 106, 2–6.

18. Liang, J., Tan, H., Liu, M., Liu, B., Wang, N., Zhang, Q., Zhao, Y., Smets, A.H.M., Zeman, M., and Zhang, X. (2016). A thin-film silicon based photocathode with a hydrogen doped TiO_2 protection layer for solar hydrogen evolution. J. Mater. Chem. A Mater. Energy Sustain. 4, 16841–16848.

19. Gu, J., Yan, Y., Young, J.L., Steirer, K.X., Neale, N.R., and Turner, J.A. (2016). Water reduction by a p-GaInP$_2$ photoelectrode stabilized by an amorphous TiO_2 coating and a molecular cobalt catalyst. Nat. Mater. 15, 456–460.

20. Hu, S., Shaner, M.R., Beardslee, J.A., Lichterman, M., Brunschwig, B.S., and Lewis, N.S. (2014). Amorphous TiO_2 coatings stabilize Si, GaAs, and GaP photoanodes for efficient water oxidation. Science 344, 1005–1009.

21. Ji, L., McDaniel, M.D., Wang, S., Posadas, A.B., Li, X., Huang, H., Lee, J.C., Demkov, A.A., Bard, A.J., Ekerdt, J.G., and Yu, E.T. (2015). A silicon-based photocathode for water reduction with an epitaxial SrTiO$_3$ protection layer and a nanostructured catalyst. Nat. Nanotechnol. 10, 84–90.

22. Kainthla, R.C. (1987). Significant Efficiency Increase in Self-Driven Photoelectrochemical Cell for Water Photoelectrolysis. J. Electrochem. Soc. 134, 841.

23. Kainthla, R.C. (1986). Protection of n-Si Photoanode against Photocorrosion in Photoelectrochemical Cell for Water Electrolysis. J. Electrochem. Soc. 133, 248.

24. Kast, M.G., Enman, L.J., Gurnon, N.J., Nadarajah, A., and Boettcher, S.W. (2014). Solution-deposited F:SnO$_2$/TiO$_2$ as a base-stable protective layer and antireflective coating for microtextured buried-junction H_2-evolving Si photocathodes. ACS Appl. Mater. Interfaces 6, 22830–22837.

25. Zhang, Z., Dua, R., Zhang, L., Zhu, H., Zhang, H., and Wang, P. (2013). Carbon-layer-protected cuprous oxide nanowire arrays for efficient water reduction. ACS Nano 7, 1709–1717.

26. Kornblum, L., Fenning, D.P., Faucher, J., Hwang, J., Boni, A., Han, M.G., Morales-Acosta, M.D., Zhu, Y., Altman, E.I., Lee, M.L., et al. (2017). Solar hydrogen production using epitaxial SrTiO3 on a GaAs photovoltaic. Energy Environ. Sci. 10, 377–382.

27. Zheng, J., Lyu, Y., Wang, R., Xie, C., Zhou, H., Jiang, S.P., and Wang, S. (2018). Crystalline TiO_2 protective layer with graded oxygen defects for efficient and stable silicon-based photocathode. Nat. Commun. 9, 3572.

28. Laursen, A.B., Pedersen, T., Malacrida, P., Seger, B., Hansen, O., Vesborg, P.C.K., and Chorkendorff, I. (2013). MoS$_2$-an integrated protective and active layer on n($^+$)p-Si for solar H_2 evolution. Phys. Chem. Chem. Phys. 15, 20000–20004.

29. Seger, B., Pedersen, T., Laursen, A.B., Vesborg, P.C.K., Hansen, O., and Chorkendorff, I. (2013). Using TiO_2 as a conductive protective layer for photocathodic H_2 evolution. J. Am. Chem. Soc. 135, 1057–1064.

30. Tan, J., Yang, W., Oh, Y., Lee, H., Park, J., Boppella, R., Kim, J., and Moon, J. (2019). Fullerene as a Photoelectron Transfer Promoter Enabling Stable TiO_2-Protected Sb$_2$Se$_3$ Photocathodes for Photo-Electrochemical Water Splitting. Adv. Energy Mater. 9, 1–12.

31. Zhang, L., Minegishi, T., Nakabayashi, M., Suzuki, Y., Seki, K., Shibata, N., Kubota, J., and Domen, K. (2015). Durable hydrogen evolution from water driven by sunlight using (Ag,Cu)GaSe$_2$ photocathodes modified with CdS and CuGa$_3$Se$_5$. Chem. Sci. (Camb.) 6, 894–901.

32. Khan, M.A., Varadhan, P., Ramalingam, V., Fu, H.C., Idriss, H., and He, J.H. (2019). Importance of oxygen measurements during photoelectrochemical water-splitting reactions. ACS Energy Lett. 4, 2712–2718.

33. Döscher, H., Geisz, J.F., Deutsch, T.G., and Turner, J.A. (2014). Sunlight absorption in water-efficiency and design implications for photoelectrochemical devices. Energy Environ. Sci. 7, 2951–2956.

34. Babaro, J.P., West, K.G., and Hamadani, B.H. (2016). Spectral response measurements of multijunction solar cells with low shunt resistance and breakdown voltages. Energy Sci. Eng. 4, 372–382.

35. Barrigón, E., Espinet-González, P., Contreras, Y., and Rey-Stolle, I. (2015). Why can't I measure the external quantum efficiency of the Ge subcell of my multijunction solar cell? AIP Conf. Proc. 1679, 050002.

36. Barrigón, E., Espinet-González, P., Contreras, Y., and Rey-Stolle, I. (2015). Implications of low breakdown voltage of component subcells on external quantum efficiency measurements of multijunction solar cells. Prog. Photovolt. Res. Appl. *23*, 1597–1607.

37. Kirchartz, T., Rau, U., Hermle, M., Bett, A.W., Helbig, A., and Werner, J.H. (2008). Internal voltages in GaInP/GaInAs/Ge multijunction solar cells determined by electroluminescence measurements. Appl. Phys. Lett. *92*, 90–93.

38. Roensch, S., Hoheisel, R., Dimroth, F., and Bett, A.W. (2011). Subcell I-V characteristic analysis of GaInP/GaInAs/Ge solar cells using electroluminescence measurements. Appl. Phys. Lett. *98*, 251113.

39. Lim, S.H., Li, J.-J., Steenbergen, E.H., and Zhang, Y.-H. (2013). Luminescence coupling effects on multijunction solar cell external quantum efficiency measurement. Prog. Photovolt. Res. Appl. *21*, 344–350.

40. Cheng, W.H., Richter, M.H., May, M.M., Ohlmann, J., Lackner, D., Dimroth, F., Hannappel, T., Atwater, H.A., and Lewerenz, H.J. (2018). Monolithic Photoelectrochemical Device for Direct Water Splitting with 19% Efficiency. ACS Energy Lett. *3*, 1795–1800.

41. Hale, G.M., and Querry, M.R. (1973). Optical Constants of Water in the 200-nm to 200-micron Wavelength Region. Appl. Opt. *12*, 555–563.

42. Pulker, H.K., Paesold, G., and Ritter, E. (1976). Refractive indices of TiO₂ films produced by reactive evaporation of various titanium-oxygen phases. Appl. Opt. *15*, 2986–2991.

43. Rakić, A.D., and Majewski, M.L. (1996). Modeling the optical dielectric function of GaAs and AlAs: Extension of Adachi's model. J. Appl. Physiol. *80*, 5909–5914.

44. Schubert, M., Gottschalch, V., Herzinger, C.M., Yao, H., Snyder, P.G., and Woolam, J.A. (1995). Optical constants of GaₓIn₁₋ₓP lattice matched to GaAs. J. Appl. Physiol. *77*, 3416.

45. Born, M., and Wolf, E. (1999). Principles of Optics, Seventh Edition (Cambridge University Press).

46. Brillet, J., Yum, J.H., Cornuz, M., Hisatomi, T., Solarska, R., Augustynski, J., Graetzel, M., and Sivula, K. (2012). Highly efficient water splitting by a dual-absorber tandem cell. Nat. Photonics *6*, 824–828.

47. Abdi, F.F., Han, L., Smets, A.H.M., Zeman, M., Dam, B., and van de Krol, R. (2013). Efficient solar water splitting by enhanced charge separation in a bismuth vanadate-silicon tandem photoelectrode. Nat. Commun. *4*, 2195.

48. Han, L., Abdi, F.F., van de Krol, R., Liu, R., Huang, Z., Lewerenz, H.J., Dam, B., Zeman, M., and Smets, A.H.M. (2014). Efficient water-splitting device based on a bismuth vanadate photoanode and thin-film silicon solar cells. ChemSusChem *7*, 2832–2838.

49. Gurudayal, S., Sabba, D., Kumar, M.H., Wong, L.H., Barber, J., Grätzel, M., and Mathews, N. (2015). Perovskite-Hematite Tandem Cells for Efficient Overall Solar Driven Water Splitting. Nano Lett. *15*, 3833–3839.

50. Sun, K., Liu, R., Chen, Y., Verlage, E., Lewis, N.S., and Xiang, C. (2016). A Stabilized, Intrinsically Safe, 10% Efficient, Solar-Driven Water-Splitting Cell Incorporating Earth-Abundant Electrocatalysts with Steady-State pH Gradients and Product Separation Enabled by a Bipolar Membrane. Adv. Energy Mater. *6*, 1–7.

51. Shi, X., Zhang, K., Shin, K., Ma, M., Kwon, J., Choi, I.T., Kim, J.K., Kim, H.K., Wang, D.H., and Park, J.H. (2015). Unassisted photoelectrochemical water splitting beyond 5.7% solar-to-hydrogen conversion efficiency by a wireless monolithic photoanode/dye-sensitised solar cell tandem device. Nano Energy *13*, 182–191.

52. Young, J.L., Steiner, M.A., Döscher, H., France, R.M., Turner, J.A., and Deutsch, T.G. (2017). Direct solar-to-hydrogen conversion via inverted metamorphic multi-junction semiconductor architectures. Nat. Energy *2*, 1–13.

53. Khaselev, O., and Turner, J.A. (1998). A monolithic photovoltaic-photoelectrochemical device for hydrogen production via water splitting. Science *280*, 425–427.

54. Kelly, N.A., and Gibson, T.L. (2006). Design and characterization of a robust photoelectrochemical device to generate hydrogen using solar water splitting. Int. J. Hydrogen Energy *31*, 1658–1673.

55. Shi, X., Jeong, H., Oh, S.J., Ma, M., Zhang, K., Kwon, J., Choi, I.T., Choi, I.Y., Kim, H.K., Kim, J.K., and Park, J.H. (2016). Unassisted photoelectrochemical water splitting exceeding 7% solar-to-hydrogen conversion efficiency using photon recycling. Nat. Commun. *7*, 11943.

56. Hu, S., Lewis, N.S., Ager, J.W., Yang, J., McKone, J.R., and Strandwitz, N.C. (2015). Thin-Film Materials for the Protection of Semiconducting Photoelectrodes in Solar-Fuel Generators. J. Phys. Chem. C *119*, 24201–24228.

57. Bae, D., Pedersen, T., Seger, B., Iandolo, B., Hansen, O., Vesborg, P.C.K., and Chorkendorff, I. (2017). Carrier-selective p- and n-contacts for efficient and stable photocatalytic water reduction. Catal. Today *290*, 59–64.

58. Pavan Kishore, V., Paramahans, P., Sadana, S., Ganguly, U., and Lodha, S. (2012). Nanocrystal-based Ohmic contacts on n and p-type germanium. Appl. Phys. Lett. *100*, 142107.

59. Yu, H., Schaekers, M., Schram, T., Aderhold, W., Mayur, A.J., Mitard, J., Witters, L., Barla, K., Collaert, N., Horiguchi, N., et al. (2016). Low-resistance titanium contacts and thermally unstable nickel germanide contacts on p-type germanium. IEEE Electron Device Lett. *37*, 482–485.

60. Nishimura, T., Kita, K., and Toriumi, A. (2007). Evidence for strong Fermi-level pinning due to metal-induced gap states at metal/germanium interface. Appl. Phys. Lett. *91*, 12–15.

61. Kang, D., Young, J.L., Lim, H., Klein, W.E., Chen, H., Xi, Y., Gai, B., Deutsch, T.G., and Yoon, J. (2017). Printed assemblies of GaAs photoelectrodes with decoupled optical and reactive interfaces for unassisted solar water splitting. Nat. Energy *2*, 1–9.